Microchimica Acta (2023) 190:407
https://doi.org/10.1007/s00604-023-05987-6

ORIGINAL PAPER

Triazine-based covalent–organic framework embedded with cuprous oxide as the bioplatform for photoelectrochemical aptasensing *Escherichia coli*

Erfu Huo[1,2] · Siyamak Shahab[3] · Hao Dang[4] · Qiaojuan Jia[4] · Minghua Wang[4]

Received: 8 June 2023 / Accepted: 4 September 2023 / Published online: 20 September 2023

Abstract

A superior photoelectrochemical (PEC) aptasensor was manufactured for the detection of *Escherichia coli* (*E. coli*) based on a hybrid of triazine-based covalent–organic framework (COF) and cuprous oxide (Cu_2O). The COF synthesized using 1,3,5-tris(4-aminophenyl)-benzene (TAPB) and 1,3,5-triformylphloroglucinol (Tp) as building blocks acted as a scaffold for encapsulated Cu_2O nanoparticles (denoted as Cu_2O@TAPB-Tp-COF), which then was employed as the bioplatform for anchoring *E. coli*-targeted aptamer. Cu_2O@Cu@TAPB-Tp-COF demonstrated enhanced separation of the photogenerated carriers and photoabsorption ability and boosted photoelectric conversion efficiency. The developed Cu_2O@TAPB-Tp-COF-based PEC aptasensor exhibited a lower detection limit of 2.5 CFU mL^{-1} toward *E. coli* within a wider range of 10 CFU mL^{-1} to 1×10^4 CFU mL^{-1} than most of reported aptasensors for determining foodborne bacteria, together with high selectivity, good stability, and superior ability and reproducibility. The recoveries of *E. coli* spiked into milk and bread samples ranged within 95.3–103.6% and 96.6–102.8%, accompanying with low RSDs of 1.37–4.48% and 1.74–3.66%, respectively. The present study shows a promising alternative for the sensitive detection of foodborne bacteria from complex foodstuffs and pathogenic bacteria-polluted environment.

Keywords Photoelectrochemical aptasensor · Foodborne bacteria · Covalent–organic framework · *Escherichia coli* · Cuprous oxide nanoparticles

Introduction

Diverse foodborne pathogenic bacteria such as *Salmonella*, *Escherichia coli* (*E. coli*), *Staphylococcus aureus* (*S. aureus*), *Vibrio parahaemolyticus*, *Botulinum*, and *Listeria* can cause foodborne diseases, seriously endangering people's lives [1]. As traditional culture-based methods are time-consuming, a variety of analysis approaches such as polymerase chain reaction (PCR) [2], enzyme-linked immunosorbent assay (ELISA) [3], and molecular imprinting technology (MIP) [4] have been extensively employed to detect foodborne pathogens [5]. In addition, different determination approaches have been developed by integrating advanced biosensing strategies established using diverse antibodies and aptamers as probes and modern means such as electrochemical approach [6], photoelectrochemical (PEC) technique [7], electrochemiluminescence [8], fluorescence [9], surface-enhanced Raman scattering (SERS), colorimetry, or paper sensor [10]. Amongst, PEC biosensing technique has been widely applied in the sensitive detection of diverse targets [11]. Comparing with PCR, ELISA, fluorescence, surface-enhanced Raman scattering (SERS), or MIP sensing methods, PEC aptasensing technique exhibits the advantages of high sensitivity, fast response, low cost, and simple equipment. Thereby, it is highly expectable for the construction of

✉ Erfu Huo
hef330@aliyun.com

✉ Minghua Wang
wangminghua@zzuli.edu.cn

1 Henan Chemical Industry Institute Co. Ltd., Zhengzhou, People's Republic of China

2 Quality Inspection and Analytical Test Research Center, Henan Academy of Sciences, Zhengzhou, People's Republic of China

3 Belarusian State University, ISEI BSU, Minsk, Republic of Belarus

4 College of Material and Chemical Engineering, Zhengzhou University of Light Industry, Zhengzhou 450001, People's Republic of China

the PEC biosensor to sensitive and rapid detection of pathogenic bacteria.

Usually, to gain the high photoelectric efficiency of PEC electrodes, semiconductors with narrow band gap such as CuO, TiO_2, SnO_2, In_2S_3, and BiOI have been used as the electrode materials [12]. However, their fast recombination rate of the photogenerated electron–hole pair hampers their applications in PEC biosensors. To address this issue, multiple components are often integrated and employed for the manufactures superior PEC biosensors to detect foodborne bacteria. Recently, covalent–organic frameworks (COFs) formed via covalent bonds often possess regular porosity, tunable structure, and enhanced chemical stability, showing the widespread applications in the fields of photo-/electrocatalysis, biosensing, and biomedicals [13]. In light of the homogeneous distributed pores, good biocompatibility, and rich functionality, COFs are widely utilized as the platforms for the fabrication of biosensors to sensitively analyze various analytes [14]. Also, due to diversified properties of COFs such as good fluorescence, wide photoabsorption ability, enhanced photoelectric conversion, or highly conjugated nanostructure, various techniques such as fluorescence, electrochemical, PEC, or electrochemiluminescence were combined with COFs for the construction of sensors [14]. Diverse COFs can be served as antibacterial platforms due to their photosensitivity, specific pore size matches, and pH-responsive release [15], but scarcely as sensing platform for the detection of foodborne pathogen. For instance, Li et al. employed a COF for loading biologic interference-free Raman reporters and specific antibodies to detect foodborne pathogens [16]. Unfortunately, no report on the COF-based PEC biosensor the detection of foodborne bacterium has been found. The utilization of COF-based photoelectrode for the construction of PEC aptasensor is still in a big challenge for the rapid, sensitive, and selective detection of foodborne bacteria.

To this end, a novel photoactive COF network confined with Cu_2O was established as the PEC platform for the sensitive and selective detection of *E. coli*. As known, *E. coli* can cause severe, hemorrhagic diarrhea, and hemolytic uremic syndrome even at a low level of 10 CFU mL^{-1} [17]. In this regard, it is essential to construct the sensitive detection method for the analysis of *E. coli* in environment or food stuffs. The COF synthesized using 1,3,5-tris(4-aminophenyl)-benzene (TAPB) and 1,3,5-triformylphloroglucinol (Tp) as building blocks was acted as the scaffold for encapsulating Cu_2O nanoparticles (denoted as Cu_2O@TAPB-Tp-COF). Given high photoelectric conversion efficiency, large porous structure, rich functionality, and encapsulation ability toward metal nanoparticles of Cu_2O@TAPB-Tp-COF, the manufactured PEC aptasensor exhibited an ultralow detection limit of 2.5 CFU mL^{-1} within a range of 10 to 1×10^4 CFU mL^{-1} toward *E. coli*, lower than most of reported electrochemical or PEC biosensors for the analysis of foodborne bacteria. The developed PEC aptasensor can provide a general aptasensing strategy for the determination of food contaminants only by replacing the corresponding aptamer strand.

Experimental

The other experimental parts are presented in the S1 section (Supporting Information), including reagents and materials, pretreatment of glass electrode (GCE), preparation of all solutions, bacterial culture, characterizations, electrochemical and photoelectrochemical measurement, and synthesis of Cu_2O and TAPB-Tp-COF.

PEC sensing mechanism

As demonstrated in Scheme 1b, due to the amplified photocurrent response, Cu_2O@TAPB-Tp-COF was selected to be served as the PEC aptasensing platform for anchoring the *E. coli*-targeted aptamer through π-π stacking, electrostatic attraction, and van der Waals forces via the two ways, including the adsorption on the surface and the penetration into the interior channels of Cu_2O@TAPB-Tp-COF. To eliminate the non-specific adsorption, the fabricated aptasensor was blocked by the bovine serum albumin (BSA, 1%). Afterwards, *E. coli* can be combined with aptamer strands immobilized over Cu_2O/TAPB-Tp-COF via specific binding based on conformational transition of aptamer. During each step of the construction of the aptasensor for the detection of *E. coli*, the photocurrent decreases owing that electron transfer at the interface of the electrode/electrolyte is inhibited. Thereby, the constructed aptasensor can be employed to detect *E. coli* through the change of the photocurrent related to the *E. coli* concentration.

Synthesis of Cu_2O@TAPB-Tp-COF

TAPB-Tp-COF was synthesized according to the reported literature [18]. The chemical structure of TAPB-Tp-COF was characterized by the ^{13}C-NMR spectrum (Fig. S1). As for the preparation of Cu_2O@TAPB-Tp-COF, TAPB-Tp-COF (20 mg) was dispersed in 3 mL of Milli-Q water under stirring for 10 min, following by adding 4 mL of $Cu(NO_3)_3{\cdot}6H_2O$ solution (2 mg mL^{-1}). After stirred for 1 h, 3 mL of $NaBH_4$ (1 mg mL^{-1}) was dropped into and kept at room temperature for 0.5 h. Finally, Cu_2O@TAPB-Tp-COF was obtained by washing with Milli-Q for several times, following by dried under vacuum at 60 °C for 8 h. Two additional hybrids were prepared by the similar approach and using the different dosages of $Cu(NO_3)_3{\cdot}6H_2O$ (4 and 16 mg), denoted as Cu_2O@TAPB-Tp-COF-1 and Cu_2O@TAPB-Tp-COF-2, respectively.

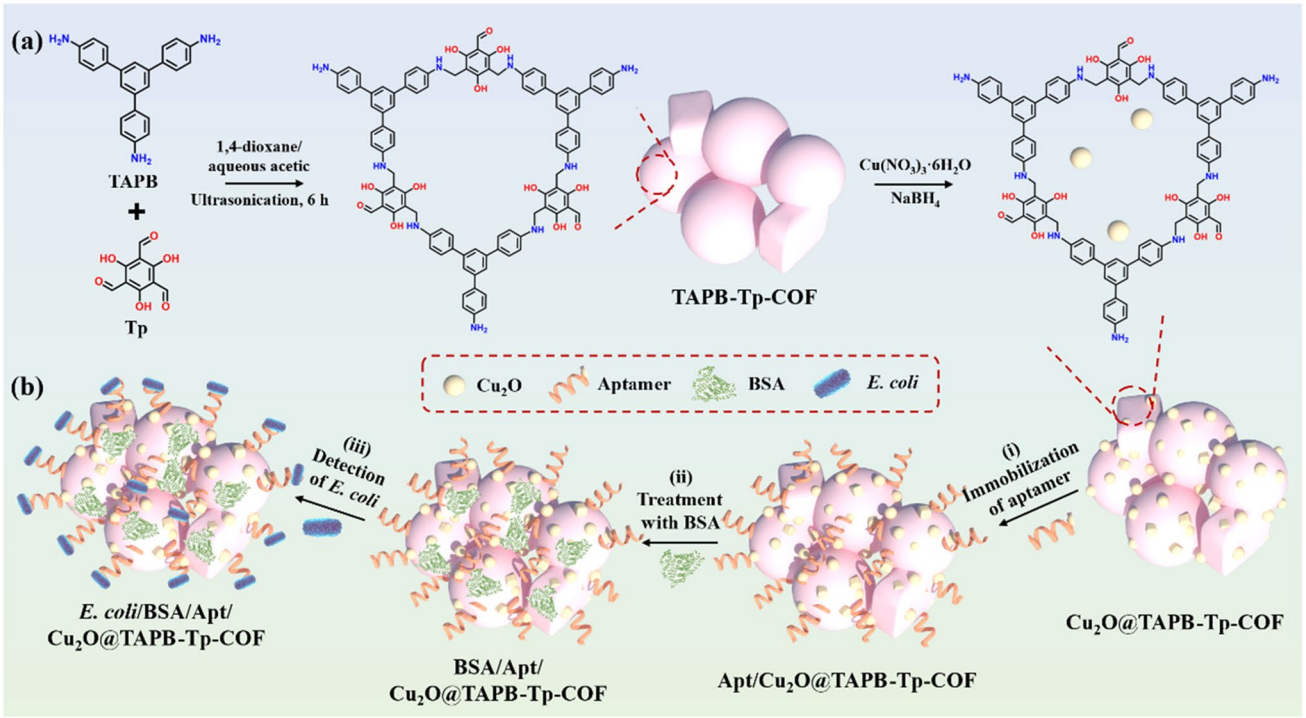

Scheme 1 **a** The synthesis route of Cu_2O@TAPB-Tp-COF and **b** fabrication of the Cu_2O@TAPB-Tp-COF-based PEC aptasensor for the detection of *E. coli*, including (i) the immobilization of aptamer strands (Apt/Cu_2O@TAPB-Tp-COF), (ii) the treatment with BSA (BSA/Apt/Cu_2O@TAPB-Tp-COF), and (iii) the detection of *E. coli* (*E. coli*/BSA/Apt/Cu_2O@TAPB-Tp-COF)

Fabrication of the PEC aptasensor

Both TAPB-Tp-COF and Cu_2O@TAPB-Tp-COF were utilized as scaffolds for anchoring aptamer to manufacture the aptasensors for the detection of *E. coli*. Firstly, TAPB-Tp-COF or Cu_2O@TAPB-Tp-COF (10 mg) was dispersed into Milli-Q water (10 mL) for the preparation of a uniform suspension with the concentration of 1 mg mL^{-1}. Afterward, 10 µL of the Cu_2O@TAPB-Tp-COF suspension was coated onto the GCE (denoted as Cu_2O@TAPB-Tp-COF/GCE). Then, the modified electrode was washed with Milli-Q water to remove the loosely attached Cu_2O@TAPB-Tp-COF. Subsequently, the Cu_2O@TAPB-Tp-COF/GCE was incubated in the aptamer solution (100 nM) for 50 min (denoted as Apt/Cu_2O@TAPB-Tp-COF/GCE). Afterward, the Apt/Cu_2O@TAPB-Tp-COF/GCE was rinsed by phosphate buffer saline (PBS, 0.01 M, pH 7.4) to remove the unbound aptamer. Prior to the detection of *E. coli*, the non-specific adsorption of *E. coli* on the Apt/Cu_2O@TAPB-Tp-COF/GCE was blocked by using BSA (represented by BSA/Apt/Cu_2O@TAPB-Tp-COF/GCE). All the prepared biosensors were stored at 4 °C for further use. For comparison, the construction of the TAPB-Tp-COF-based aptasensor was carried out by the similar method by replacing Cu_2O@TAPB-Tp-COF with TAPB-Tp-COF.

The detection of E. coli using the Cu_2O@ TAPB-Tp-COF-based aptasensor

The development of the aptasensor and the analysis of *E. coli* were investigated by using the PEC technique. Prior to the investigation of the aptasensing performance toward *E. coli*, the determination conditions were optimized, including the concentration of Cu_2O@TAPB-Tp-COF, the aptamer concentration, the adsorption time of aptamer, and the binding time of *E. coli* with aptamer. Under the optimal conditions, the limit of detection (LOD) of the proposed aptasensor was studied by separately detecting different concentrations of *E. coli* (10, 50, 100, 500, 1×10^3, 5×10^3, and 1×10^4 CFU mL^{-1}). By taking the variation of the photocurrent response ($\Delta I = I_{E.\ coli} - I_{BSA}$), which represents photocurrent of the modified electrode before and after the detection of *E. coli*) as the function of the logarithm of the *E. coli* concentration ($lgCon_{E.\ coli}$), the LOD of the PEC aptasensor was deduced.

Moreover, to investigative the selectivity of the fabricated aptasensor, varieties of other kinds of bacteria, which are possibly existed together with *E. coli* in foodstuffs, including *Bacillus subtilis* (*B. subtilis*), *S. aureus*, *Salmonella* typhimurium (*S. typhimurium*), and their mixtures with *E. coli*, were used to detect *E. coli*. The concentration of these interferents and their mixture with *E. coli* was 1×10^4 CFU mL^{-1},

which was 100-fold of *E. coli* (100 CFU mL^{-1}). In addition, the reproducibility of the aptasensor was investigated via the analysis of *E. coli* (100 CFU mL^{-1}) using five same fresh BSA/Apt/Cu_2O@TAPB-Tp-COF/GCEs. The stability was evaluated by continuously recording the PEC responses for the analysis of *E. coli* (100 CFU mL^{-1}) using the same PEC aptasensor.

Further, the regeneration ability was measured by immersing the *E. coli*/BSA/Apt/Cu_2O@TAPB-Tp-COF/GCE in 100 mM NaOH for 2 min at room temperature, followed by rinsing with excess PBS (0.01 M, pH 7.4). Therefore, the aptamer–*E. coli* complex could be dissociated, resulting in the removal of *E. coli*. The refreshed electrode was immersed into *E. coli* solution (100 CFU mL^{-1}) again until the photocurrent response was up to the original level. The whole regeneration procedure was repeated by 15 cycles to evaluate the regeneration ability of the developed aptasensor.

Real samples

To assess the applicability of the developed aptasensor, it was used to detect *E. coli* commonly containing in food samples (such as raw milk and bread). Raw milk and bread were purchased from a local supermarket. Before used, 10 g of bread was put into sterile homogeneous bag containing 10 mL of PBS (0.01 mM pH 7.4) and sonicated for 10 min to obtain bread sample. As for milk sample, 0.2 mL of NaOH (100 mM) and 0.8 mL of acetonitrile were mixed with the sample in a centrifuge tube. Then, these milk samples were centrifuged for 5 min at rotating speed of 5000 rpm min^{-1} for the removal of biological impurities (such as proteins and lipids proteins). All pretreated real samples were diluted 100 times with PBS (0.01 M, pH 7.4) and sterilized in an autoclave for further use. *E. coli* was diluted to different concentrations (10, 50, 100, 500, 1×10^3, 5×10^3, and 1×10^4 CFU mL^{-1}) with the treated milk and bread supernatants to form real sample solutions.

Results and discussion

Choice of materials

Given porous structured COF-based substrates have demonstrated the tunable components, regular skeleton, high functionality, and large specific surface area and pore size, it could afford the enhanced bioaffinity toward bioprobes such as antibodies, DNAs, and aptamers [19]. In addition, COFs with highly conjugated structure usually exhibit the improved UV–vis light adsorption ability. By integrating with photoactive Cu_2O nanomaterials, the band gap of COFs can be narrowed, which thus boosts the photogenerated carrier transfer and promotes the photoelectrochemical response. In this work, TAPB-Tp-COF synthesized using TAPB and Tp as building blocks was combined with Cu_2O to serve as the PEC electrode material. And the photoelectrochemical signal of the Cu_2O@TAPB-Tp-COF-modified electrode and the aptamer immobilization capability can be optimized by tuning the dosage of TAPB-Tp-COF for attaining the superior aptasensing performance toward *E. coli*.

Basic characterizations of Cu_2O@TAPB-Tp-COF

As depicted in the field emission scanning electron microscopy (FE-SEM) image of Cu_2O@TAPB-Tp-COF (Fig. 1a), the nanosphere-like shape is maintained but showing a certain aggregation and accompanying with some small particles. The transmission electron microscopy (TEM) image of Cu_2O@TAPB-Tp-COF (Fig. 1b) shows some deep black particles are entrapped within COF nanospheres. An apparent lattice spring with the distance of 0.242 nm in the high-resolution TEM image (Fig. 1c) corresponds to Cu_2O (111) crystal face [20]. The energy-dispersive X-ray spectroscopy (EDX) image of Cu_2O@TAPB-Tp-COF (Fig. 1d) demonstrates the homogeneous dispersion of C, N, O, and Cu elements.

The powder X-ray diffraction (PXRD) pattern of TAPB-Tp-COF (Fig. 1e, curve *i*) indicates there is no significant diffraction peak. However, a weak diffraction peak at $2\theta = 36.4°$ is gained in the XRD pattern of Cu_2O@TAPB-Tp-COF (Fig. 1e, curve *ii*), which is indexed to Cu_2O (JCPDS#05–0667). As indicated in the Fourier transform infrared (FT-IR) spectrum of TAPB-Tp-COF (Fig. 1f), the peak located at 1580 cm^{-1} is assigned to C = N vibration band. Notably, the two peaks of 3433 and 3353 cm^{-1} corresponded to N–H vibration bond in TAPB, and the peak at 1668 cm^{-1} due to C = O bond is absent. The similar FT-IR spectrum of Cu_2O@TAPB-Tp-COF can be found, hinting the incorporation of Cu_2O into the porous TAPB-Tp-COF network cannot change its chemical structure. The typical features of type IV isotherms with H3 hysteresis loop in the nitrogen sorption and desorption curves of TAPB-Tp-COF Cu_2O@TAPB-Tp-COF indicate their mesopore structure (Fig. 1g). Further, TAPB-Tp-COF has a larger Brunauer–Emmett–Teller surface area (193 $m^2\ g^{-1}$) than that of Cu_2O@TAPB-Tp-COF (47.6 $m^2\ g^{-1}$) due to the introduction of Cu_2O nanoparticles. However, the average pore diameter obtained by fitting the Barrett–Joyner–Halenda (BJH) model to the nitrogen desorption plot of TAPB-Tp-COF is around 11.5 nm, smaller than that of Cu_2O@TAPB-Tp-COF (19.9 nm). The large specific surface area and pore size of Cu_2O@TAPB-Tp-COF can expose the binding sites toward aptamer.

Figure 2a shows the Cu 2*p* high-resolution XPS spectrum of Cu_2O@TAPB-Tp-COF comprises Cu $2p_{3/2}$ and

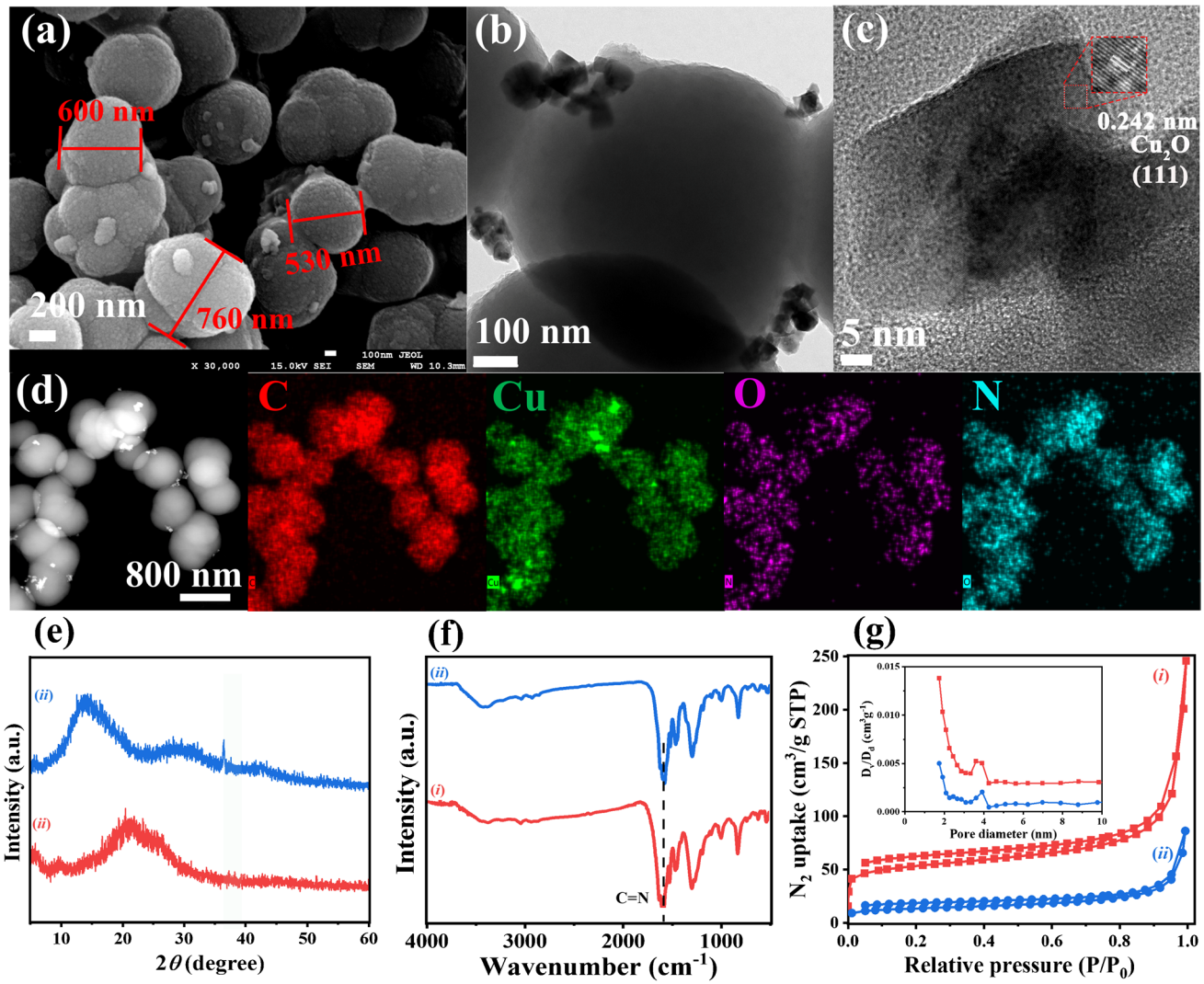

Fig. 1 **a–c** FE-SEM, TEM, and HR-TEM images, **d** HAAD-STEM image and corresponding EDX element mapping images of Cu_2O@TAPB-Tp-COF (C (red), Cu (green), O (purple), and N (blue)). **e** XRD, **f** FT-IR, and **g** N_2 adsorption/desorption isotherms (*i*) TAPB-Tp-COF and (*ii*) Cu_2O@TAPB-Tp-COF

Cu $2p_{1/2}$, which are fitted into Cu^{2+} (936.1 and 953.1 eV) and Cu^{+} (934.2 and 954.2 eV), together with their satellite peaks. The C 1 *s* XPS spectrum of includes four groups of C–C (284.6 eV), C-N (286.1 eV), COO (288.1 eV), and π-π* (290.9 eV) (Fig. 2b), in which π-π* bond hints the highly conjugated structure of Cu_2O@TAPB-Tp-COF. As depicted in Fig. 2c, pyrrolic N (399.3 eV) and graphitic N (400.1 eV) species are composed in the N 1 *s* XPS spectrum, originating from triazine structure. Notably, the O 1 *s* XPS spectrum (Fig. 2d) can be deconvoluted into oxygen vacancy (530.4 eV), C = O (531.5 eV), C-O (532.8 eV), and adsorbed O (535.8 eV). It is apparent that Cu–O in Cu_2O (Fig. S5b) is not present in the Cu_2O@TAPB-Tp-COF heterojunction, hinting the full entrapment of Cu_2O within the porous COF network.

Evaluation of the photoelectrochemical performance of Cu_2O@TAPB-Tp-COF

As illustrated in Fig. 3a, the Mott–Schottky curve slopes of TAPB-Tp-COF and Cu_2O are positive, revealing their features of n-type semiconductors. Furthermore, the flat band potentials (E_{fb}) of all samples versus (vs.) to the AgCl electrode (statured KCl solution) were obtained by drawing a tangent line from Mott–Schottky curve. Accordingly, the E_{fb} values of TAPB-Tp-COF and Cu_2O are − 0.37 and − 0.34 V, respectively. Accordingly, the E_{fb} vs. normal hydrogen electrode (NHE) of TAPB-Tp-COF and Cu_2O are − 0.17 V and − 0.14 V, respectively. As the potential of conduction band (E_{CB}) or the lowest unoccupied molecular orbital (LUMO) is negative 0.2 V than

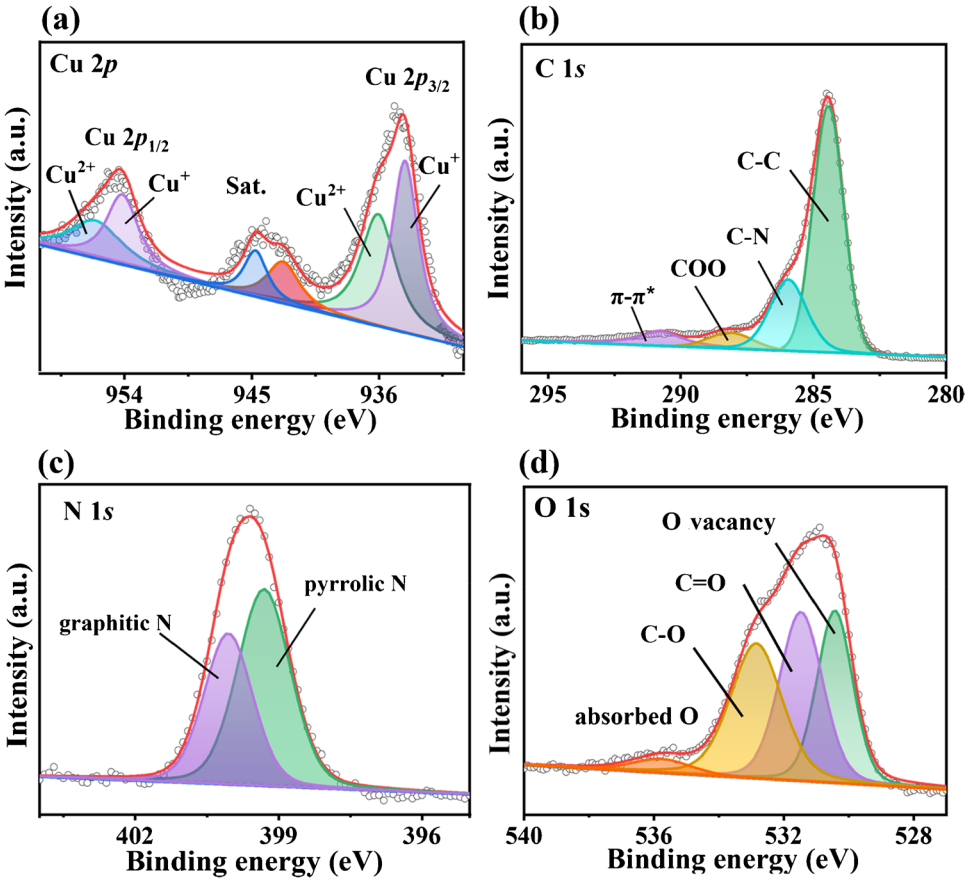

Fig. 2 High-resolution **a** Cu 2*p*, **b** C 1 *s*, **c** N 1 *s*, and **d** O 1 *s* XPS spectra of Cu_2O@TAPB-Tp-COF

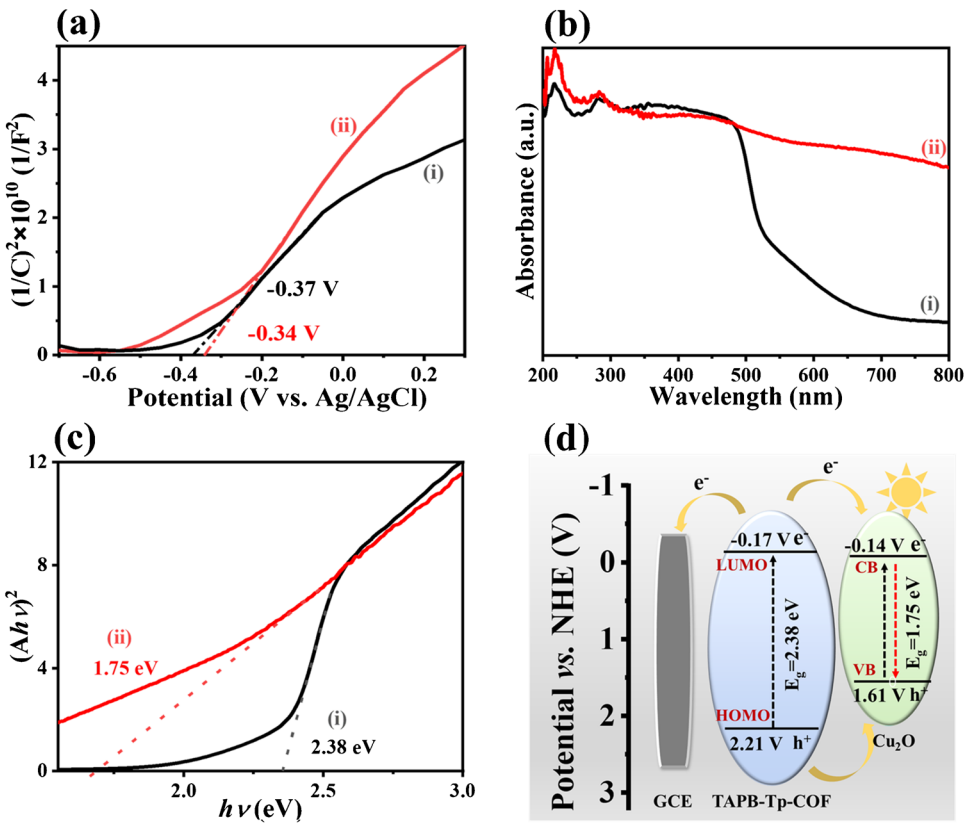

Fig. 3 **a** Mott–Schottky plots, **b** UV–vis DRS spectra, and **c** corresponding to Tauc plots of (i) TAPB-Tp-COF and (ii) Cu_2O. **d** Schematic illustration of the PEC process on Cu_2O@TAPB-Tp-COF

E_{fb}, the E_{LUMO} of TAPB-Tp-COF is − 0.37 V, while the E_{CB} of Cu_2O is − 0.34 V. To figure out the valence band potential (E_{VB}), the UV–visible diffuse reflection (UV-DRS) spectra of Cu_2O and TAPB-Tp-COF were measured (Fig. 3b). The band gap (E_g) of Cu_2O and TAPB-Tp-COF was derived from the Tauc-plot (Fig. 3c), being 1.75 and 2.38 eV, respectively. Furthermore, based on the equation ($E_{VB} = E_g$-E_{CB}), the potential of VB and the highest occupied molecular orbital (HOMO) of Cu_2O and TAPB-Tp-COF were calculated to be 1.61 and 2.21 V, respectively. Based on the above results, the energy level of HOMO and LUMO of TAPB-Tp-COF is at lower level than the energy level of the VB and CB of Cu_2O (Fig. 3d). Consequently, the migration of the photo-induced e^- and hole (h^+) between TAPB-Tp-COF and Cu_2O heterojunction can be promoted, forming the type I heterojunction. Under visible light irradiation, the photogenerated electrons and holes of TAPB-Tp-COF transfer to the CB and VB of Cu_2O, respectively. Additionally, photogenerated electrons of TAPB-Tp-COF also transfer to the GCE, thus generating an anode photocurrent response. The produced h^+ of Cu_2O is consumed by electron–hole pairs. Hence, a high pathway of photogenerated electron–hole pairs can be established between TAPB-Tp-COF and Cu_2O, markedly boosting the change transfer and quenched photocurrent signaling. It thus provides the promising applications of Cu_2O@TAPB-Tp-COF to be utilized as the PEC biosensor platform with the amplified output sensing signal [21].

PEC performance of Cu_2O@TAPB-Tp-COF

The construction procedure of the Cu_2O@TAPB-Tp-COF-based aptasensor was simultaneously probed by PEC and EC techniques. Figure 4a indicates the Cu_2O@TAPB-Tp-COF/GCE demonstrates an amplified photocurrent density (0.53 μA) comparing with the TAPB-Tp-COF/GCE (0.28 μA). This finding reveals the recombination of photogenerated electrons and holes can be effectively suppressed on Cu_2O@TAPB-Tp-COF. After the Cu_2O@TAPB-Tp-COF/GCE was incubated with the aptamer solution (100 nM), the corresponding photocurrent density declines to 0.30 μA. Distinctly, the aptamer immobilization over Cu_2O@TAPB-Tp-COF can increase the hindrance effect on charge transfer at the interfacial between electrolyte and the GCE. In addition, the clear P 2*p* XPS signal (Fig. S10) can be achieved in the Apt/Cu_2O@TAPB-Tp-COF complex, which is originated from the phosphate group bearing on aptamer. Notably, blocking with BSA cannot cause the significant decrease in the photocurrent density, revealing that unsubstantial non-specific binding between target with the platform. When detecting *E. coli*, the generated complex of *E. coli*–aptamer over the photoelectrode surface substantially results in the decrease of the photocurrent (0.23 μA). It can be attributed to the change of surface structure and poor conductivity of the complex layer. Also, it increases the steric hindrance, inhibiting electron transfer to the electrode surface and reducing the photocurrent.

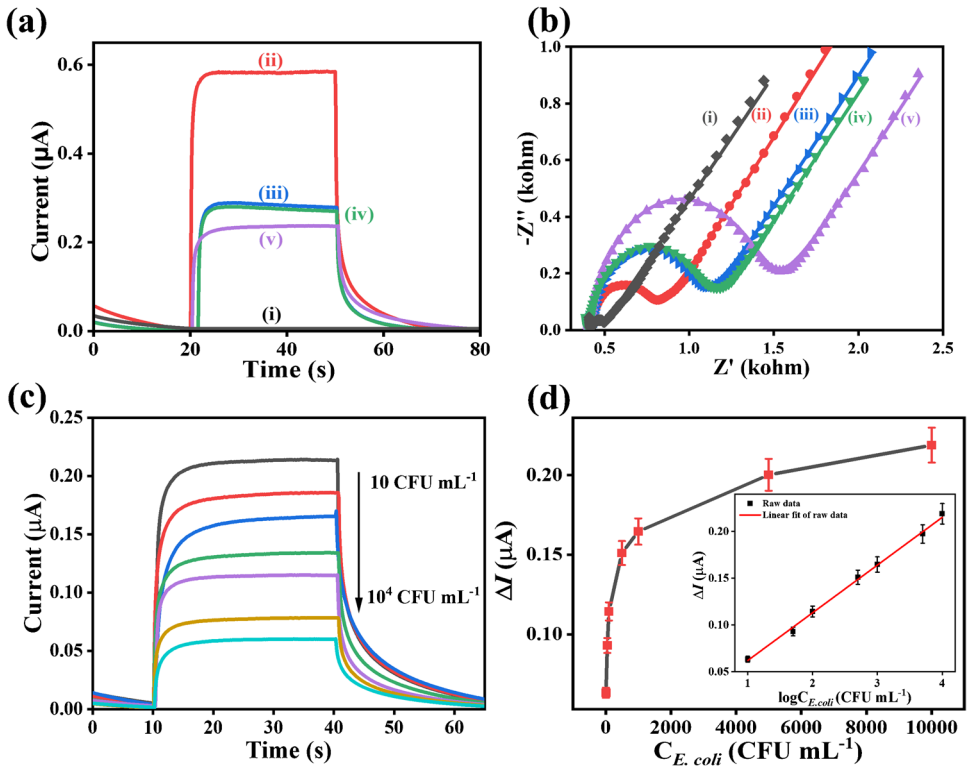

Fig. 4 **a** Photocurrent responses and **b** EIS Nyquist plots recorded by the construction procedure of the Cu_2O@TAPB-Tp-COF-based aptasensor and the detection of *E. coli* (10 CFU mL^{-1}). **c** Photocurrent responses for the detection of *E. coli* with different concentrations (10, 50, 100, 500, 1×10^3, 5×10^3, and 1×10^4 CFU $mL.^{-1}$) using the Cu_2O@TAPB-Tp-COF-based aptasensor. **d** Calibration curve between ΔI and the *E. coli* concentration (inset: the linear fit plot of ΔI as a function of the logarithm of *E. coli* concentration)

Meanwhile, the electrochemical impedance spectroscopy (EIS) Nyquist plots of the construction of the Cu_2O@TAPB-Tp-COF-based aptasensor are shown in Fig. 4b. The bare GCE has a small resistance of charge transfer (R_{ct}, 85 Ω), suggesting its excellent electrochemical conductivity. The Cu_2O/GCE shows the R_{ct} (506.7 Ω), smaller than that of the TAPB-Tp-COF/GCE (551.9 Ω), hinting its outperformed electrochemical activity. Further, the Cu_2O@TAPB-Tp-COF/GCE shows an even smaller R_{ct} value (396.8 Ω) than that of the TAPB-Tp-COF/GCE, verifying the enhanced electrochemical activity by introducing Cu_2O nanoparticles. Further, the Apt/Cu_2O@TAPB-Tp-COF/GCE results in a larger R_{ct} (652.5 Ω) than that of Cu_2O@TAPB-Tp-COF/GCE. It is due to the increased steric hindrance for electron transfer caused by the aptamer immobilization at the interface of the electrolyte/electrode. Subsequently, the BSA/Apt/Cu_2O@TAPB-Tp-COF/GCE demonstrates a slightly increased R_{ct} value (670.4 Ω). In the presence of *E. coli*, the *E. coli*/BSA/Apt/Cu_2O@TAPB-Tp-COF/GCE shows an apparently increased R_{ct} (1012.5 Ω). It is ascribed to the change of surface structure and poor conductivity of the complex layer on the electrode. These results confirm that the qualitative analysis of *E. coli* can be realized by the manufactured Cu_2O@TAPB-Tp-COF-based aptasensor.

To gain the superior detection performance, some experimental conditions or parameters have been optimized in advance. As indicated in Figs. S11 and S12 and described in the S3 section, the optimal parameters can be summarized as the usage of Cu_2O@TAPB-Tp-COF for the modification of the GCE of 1.5 mg mL^{-1}, the aptamer concentration of 100 nM, the adsorption time of aptamer of 50 min, and the binding time of *E. coli* of 40 min.

Qualitative analysis of the developed PEC aptasensor

Under the optimal conditions, the analysis sensitivity of the constructed PEC aptasensor based on Cu_2O@TAPB-Tp-COF was investigated according to the concentration titration method within the *E. coli* concentration ranging from 10 to 1×10^4 CFU mL^{-1}. Figure 4c demonstrates the photocurrent decreases with increasing the *E. coli* concentration. The caused variation in the photocurrent (ΔI) dramatically increases from 63 nA to 0.22 μA with increasing the *E. coli* concentration from 10 to 1×10^4 CFU mL^{-1}, revealing the increasing formation of the complex of *E. coli*/aptamer. When the *E. coli* concentration is larger than 1×10^4 CFU mL^{-1}, the ΔI approaches to a platform, hinting the saturated combination of *E. coli* and immobilized aptamer. A well linear relationship is found between the ΔI and the logarithm of the *E. coli* level ($lgC_{E.coli}$) and can be represented by ΔI (nA) = 11 + 51$lgC_{E.coli}$ (CFU mL^{-1}) within a range of 10 to 1×10^4 CFU mL^{-1} (Fig. 4d). According to 3 *S*/K, where *S* represents the standard deviation of 10 measurements of the blank sample without oligos ($n=10$) and *K* indicates the slope of the standard curve [22], an ultralow LOD of 2.5 CFU mL^{-1} can be deduced. Clearly, the manufactured PEC aptasensor demonstrates the substantially lower LOD than those of previous PEC aptasensors for the detection of foodborne pathogens (Table 1). As aforementioned, Cu_2O@TAPB-Tp-COF exhibits plenty of amino moieties, oxygen vacancies, and abundant active sites, greatly facilitating large amounts of aptamer strands to anchor. In addition, coupling Cu_2O nanoparticles and porous nanostructure of COF can result in the excellent electrochemical activity and high photoelectronic conversion rate of Cu_2O@TAPB-Tp-COF, thus enlarging the PEC detection response.

Table 1 Comparison of the linear range and LOD of our work for *E. coli* detection with previously reported work

Materials	Detection method	Detection range (CFU mL^{-1})	LOD (CFU mL^{-1})	Refs
Au-Cys-Ab	EIS	$3–3\times10^7$	30	[23]
CQDs-MNPs	Fluorescence	$500–1\times10^6$	487	[24]
CDs@colistin-3	Fluorescence	$381–2.44\times10^4$	460	[25]
Pt–Au NPs	Immunochromatographic	$10–1\times10^8$	100	[26]
Polymer	Microcontact imprinting	$100–1\times10^7$	70	[27]
AuNPs	Colorimetric	$50–5\times10^4$	50	[28]
p-Benzoquinone	Cyclic voltammetry	1×10^3 to 1×10^9	1000	[29]
pAb-N-GQDs	Electrochemiluminescence	$10–1\times10^7$	8	[30]
$AgBiS_2/Cu_2O$	PEC	$25–5\times10^7$	8	[7]
Cu_2O@TAPB-Tp-COF	PEC	$10–1\times10^4$	2.5	This work

Specificity, reproducibility, stability, and regeneration performance of the Cu_2O@TAPB-Tp-COF-based PEC aptasensor

The specificity of the manufactured PEC aptasensor was estimated by detecting diverse interferents (*E. coli DH5α*, *B. subtilis*, *S. typhimurium*, and *S. aureus*) and their mixture with *E. coli*, which could be co-existed with *E. coli* in real samples. The concentration of used interferents was set as 1×10^4 CFU mL^{-1}, 100-fold of the *E. coli* (100 CFU mL^{-1}). The gained variations of the photocurrent for the determination of interferents, *E. coli*, and their mixture are illustrated in Fig. 5a. It shows the insignificant Δ*I* signals caused by the analysis of the interferents, while the detection of the mixed samples demonstrates the comparable response with that of the analysis of *E. coli*. These appearances hint that the present PEC aptasensor has a high selectivity for the analysis of *E. coli* from the complex environment. In addition, five same PEC aptasensors have been developed to analyze the same sample for the judgment of reproducibility. Figure 5b indicates the deduced Δ*I* signals originated from the determination of *E. coli* are very close, showing the relative standard deviation (RSD) of 1.83%. It manifests the ascendant reproducibility of the established PEC aptasensor. Moreover, the storage ability of the provided aptasensor was appraised by recording the Δ*I* responses each day for continuously measuring for 20 days using the same aptasensor. As indicated in Fig. 5c, the relatively equivalent Δ*I* signals can be gained, demonstrating the RSD of 2.46%. It insinuates the good stability of the developed aptasensor for long-term storage. Notably, the engineered PEC aptasensor also displays the expected revived ability to cut the fabrication cost and construction procedure. As indicated in Fig. 5d, when refreshed the used aptasensor for the first time, the photocurrent variation returns to 0.295 μA, which is close to the fresh one. After the detection of *E. coli* again, it can cause

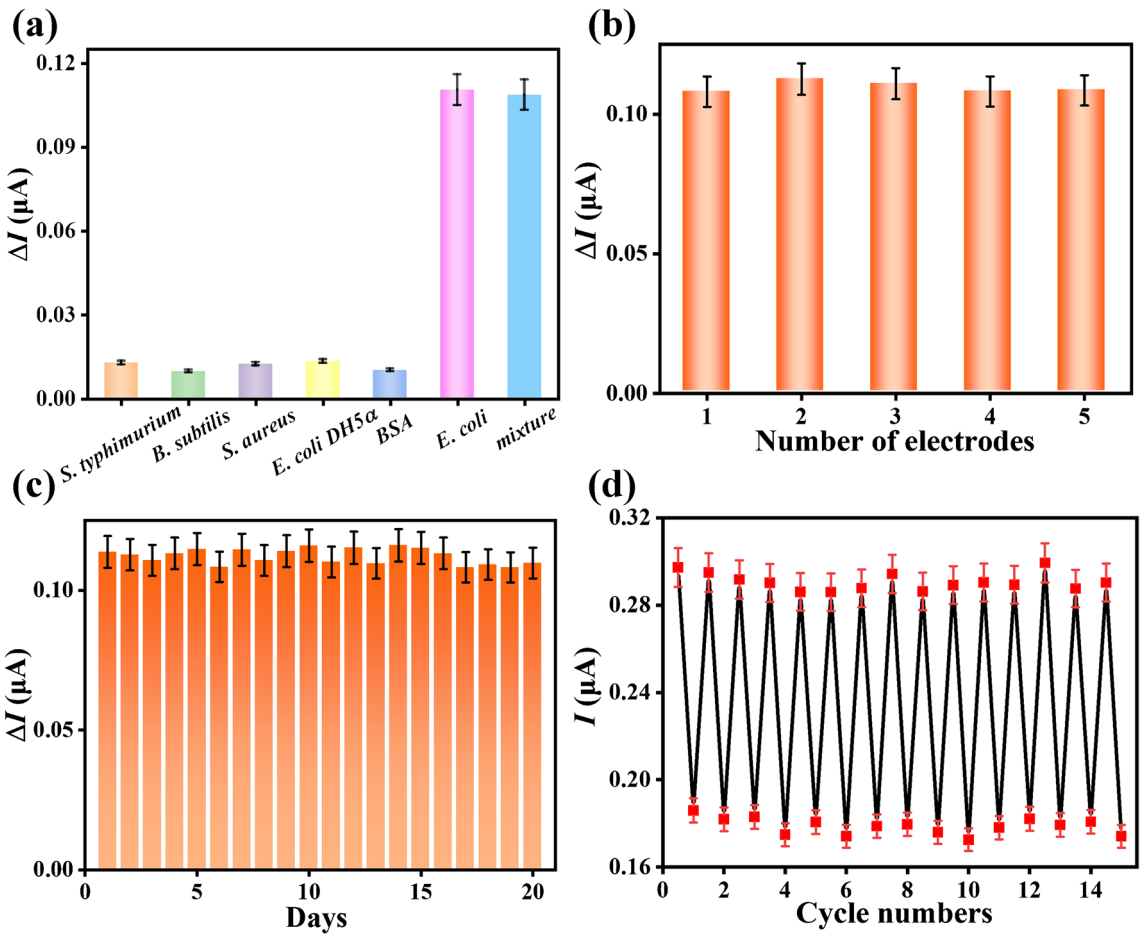

Fig. 5 **a** Photocurrent responses for the detection of *E. coli* (100 CFU mL^{-1}) and *E. coli DH5α*, *B. subtilis*, *S. typhimurium*, *S. aureus,* (1×10^4 CFU mL^{-1}), and BSA, as well as the mixture of *E. coli* and all interferents (1×10^4 CFU mL^{-1}). **b** Photocurrent responses of the five independent Cu_2O@TAPB-Tp-COF-based aptasensor for detecting *E. coli* (100 CFU mL^{-1}). **c** Photocurrent responses of the same aptasensor for the detection of *E. coli* (100 CFU mL^{-1}) per day for 20 days. The error bars are standard deviations for $n=3$. **d** The regenerability of the Cu_2O@TAPB-Tp-COF-based aptasensor

the decrease of the photocurrent to 0.182 μA, leading to the ΔI of 0.113 μA. This finding denotes that the regenerated PEC aptasensor has a superior recycling ability. The whole procedure for the construction of the PEC can be recycled for 15 times, reserving the signal of 97.3% of the initial one. The above aptasensing performances of the constructed PEC biosensor based on Cu_2O@TAPB-Tp-COF afford the great potential real applications.

Practicality

Based on the above superior biosensing abilities of the constructed PEC aptasensor, the assessment of its practicality in the detection of *E. coli* was performed in raw milk and bread. All real samples were pretreated according to the detailed description in the "Real samples" section. After spiking different concentrations of *E. coli* into these samples, the actual level of *E. coli* was determined using the manufactured aptasensor and compared with the added values. All results are summarized in Tables S1-S2. As for the analysis of *E. coli* in raw milk, the recoveries are ranged from 95.3 to 103.6%, accompanying with the low RSDs of 1.37–4.48%. Similarly, the relative comparable recoveries of bread are observed in the detection of *E. coli* in 96.6–102.8%, respectively, along with the low RSDs of 1.74–3.66%. Also, the level of *E. coli* in diverse real samples was also determined by plate count method. Fig. S13 depicts the comparable results with those detected by the proposed aptasensor. These findings can purport the acceptable and extensive applications of the developed aptasensor.

Conclusion

We have proposed a new PEC aptasensor based on the organic–inorganic hybrid for the sensitive analysis of *E. coli*. The efficient heterojunction of Cu_2O@TAPB-Tp-COF was generated via the incorporation of Cu_2O nanoparticles into the highly porous TAPB-Tp-COF network. As compared with the PEC aptasensors for the detection foodborne bacteria, the currently developed aptasensor demonstrated the three advantages: (i) the large specific surface area and functionality of TAPB-Tp-COF afforded high bioaffinity toward aptamer, resulting in large amounts of aptamer anchored; (ii) the junction of inorganic Cu_2O nanoparticles and TAPB-Tp-COF simultaneously facilitated the separation ability of electrons and holes and stabilized the aptamer–*E. coli* complex, improving the sensing ability; and (iii) the enhanced solution stability of Cu_2O@TAPB-Tp-COF provided the regenerated ability of the constructed aptasensor, extenuating the manufacture cost and detection procedure. The manufactured PEC aptasensor based on Cu_2O@TAPB-Tp-COF gave an ultralow LOD toward *E. coli* within a wide range. However, the fabricated Cu2O@TAPB-Tp-COF-based aptasensor still illustrated some limitations, such as the fussy preparation of the aptasensor, somehow limiting its widespread application. This work can propose a good PEC aptasensor based on COF for the sensitive analysis of food containments.

Supplementary Information The online version contains supplementary material available at https://doi.org/10.1007/s00604-023-05987-6.

Acknowledgements The authors gratefully thank the Analytical and Testing Center of Zhengzhou University and Henan Province Analysis and Test Center for NMR measurements.

Funding This work was supported by the Henan Province High-End Foreign Experts Introduction Plan (No. HNGD2023034).

Data Availability Data will be made available on request.

Declarations

Conflict of interest The authors declare no competing of interests.

References

1. Peltomaa R, Benito-Peña E, Gorris HH, Moreno-Bondi MC (2021) Biosensing based on upconversion nanoparticles for food quality and safety applications. Analyst 146:13–32. https://doi.org/10.1039/D0AN01883J
2. Tao J, Liu W, Ding W, Han R, Shen Q, Xia Y, Zhang Y, Sun W (2020) A multiplex PCR assay with a common primer for the detection of eleven foodborne pathogens. J Food Sci 85:744–754. https://doi.org/10.1111/1750-3841.15033
3. Pang B, Zhao C, Li L, Song X, Xu K, Wang J, Liu Y, Fu K, Bao H, Song D, Meng X, Qu X, Zhang Z, Li J (2018) Development of a low-cost paper-based ELISA method for rapid *Escherichia coli* O157:H7 detection. Anal Biochem 542:58–62. https://doi.org/10.1016/j.ab.2017.11.010
4. Zhang J, Wang Y, Lu X (2021) Molecular imprinting technology for sensing foodborne pathogenic bacteria. Anal Bioanal Chem 413:4581–4598. https://doi.org/10.1007/s00216-020-03138-x
5. Rohde A, Hammerl JA, Boone I, Jansen W, Fohler S, Klein G, Dieckmann R, Al Dahouk S (2017) Overview of validated alternative methods for the detection of foodborne bacterial pathogens. Trends Food Sci Tech 62:113–118. https://doi.org/10.1016/j.tifs.2017.02.006
6. Castle LM, Schuh DA, Reynolds EE, Furst AL (2021) Electrochemical sensors to detect bacterial foodborne pathogens. ACS Sensors 6:1717–1730. https://doi.org/10.1021/acssensors.1c00481
7. Chen X, Yin M, Ge R, Wei J, Jiao T, Chen Q, Oyama M, Chen Q (2023) Insight into a target-induced photocurrent-polarity-switching photoelectrochemical immunoassay for ultrasensitive detection of *Escherichia coli* O157:H7. Anal Chem 95:2698–2705. https://doi.org/10.1021/acs.analchem.2c03235
8. Tao Q, Tang N, Jiang Y, Chen B, Liu Y, Xiong X, Liu S (2023) Double bipolar electrode electrochemiluminescence color switch for food-borne pathogens detection. Biosens Bioelectron 237:115452. https://doi.org/10.1016/j.bios.2023.115452
9. You H, Wang M, Wang S, Xu J, Hu S, Li T, Yu Z, Tang D, Gan N (2023) Ultrasensitive and specific phage@DNAzyme probe-triggered fluorescent click chemistry for on-site detection of foodborne pathogens using a smartphone. Anal Chem 95:11211–11218. https://doi.org/10.1021/acs.analchem.3c00603

10. Bai Z, Xu X, Wang C, Wang T, Sun C, Liu S, Li D (2022) A comprehensive review of detection methods for *Escherichia coli* O157:H7. TrAC Trends Anal Chem 152:116646. https://doi.org/10.1016/j.trac.2022.116646
11. Tu W, Wang Z, Dai Z (2018) Selective photoelectrochemical architectures for biosensing: design, mechanism and responsibility. TrAC Trends Anal Chem 105:470–483. https://doi.org/10.1016/j.trac.2018.06.007
12. Liu X, Jiang Y, Luo J, Guo X, Ying Y, Wen Y, Yang H, Wu Y (2021) A SnO_2/Bi_2S_3-based photoelectrochemical aptasensor for sensitive detection of tobramycin in milk. Food Chem 344:128716. https://doi.org/10.1016/j.foodchem.2020.128716
13. Ding S-Y, Wang W (2013) Covalent organic frameworks (COFs): from design to applications. Chem Soc Rev 42:548–568. https://doi.org/10.1039/C2CS35072F
14. Zhang X, Li G, Wu D, Zhang B, Hu N, Wang H, Liu J, Wu Y (2019) Recent advances in the construction of functionalized covalent organic frameworks and their applications to sensing. Biosens Bioelectron 145:111699. https://doi.org/10.1016/j.bios.2019.111699
15. Mal A, Ding H, Li M, Li W, Wang C (2022) Covalent organic frameworks with nanopores for biological applications: a review. ACS Appl Nano Mater 5:13972–13984. https://doi.org/10.1021/acsanm.2c01517
16. Yang Y, Li G, Wang P, Fan L, Shi Y (2022) Highly sensitive multiplex detection of foodborne pathogens using a SERS immunosensor combined with novel covalent organic frameworks based biologic interference-free Raman tags. Talanta 243:123369. https://doi.org/10.1016/j.talanta.2022.123369
17. Bystrom PV, Beck RJ, Prahlow JA (2017) Hemolytic uremic syndrome caused by *E. coli* O157 infection. Forensic Sci Med Pat 13:240–244. https://doi.org/10.1007/s12024-017-9852-y
18. Gan S-X, Jia C, Qi Q-Y, Zhao X (2022) A facile and scalable synthetic method for covalent organic nanosheets: ultrasonic polycondensation and photocatalytic degradation of organic pollutants. Chem Sci 13:1009–1015. https://doi.org/10.1039/D1SC05504F
19. Yuan R, Li H-K, He H (2021) Recent advances in metal/covalent organic framework-based electrochemical aptasensors for biosensing applications. Dalton Trans 50:14091–14104. https://doi.org/10.1039/D1DT02360H
20. Zhu J, Jiang E, Wang X, Pan Z, Xu X, Ma S, Kang Shen P, Pan L, Eguchi M, Nanjundan AK, Shapter J, Yamauchi Y (2022) Gram-scale production of Cu_3P-Cu_2O Janus nanoparticles into nitrogen and phosphorous doped porous carbon framework as bifunctional electrocatalysts for overall water splitting. Chem Eng J 427:130946. https://doi.org/10.1016/j.cej.2021.130946
21. Gao Y, Zeng Y, Liu X, Tang D (2022) Liposome-mediated in situ formation of type-I heterojunction for amplified photoelectrochemical immunoassay. Anal Chem 94:4859–4865. https://doi.org/10.1021/acs.analchem.2c00283
22. Liu R, Haruna SA, Ali S, Xu J, Zhang Y, Lü P, Li H, Chen Q (2022) A sensitive and accurate fluorescent genosensor for *Staphylococcus aureus* detection. Sens Actuators B Chem 355:131311. https://doi.org/10.1016/j.snb.2021.131311
23. Malvano F, Pilloton R, Albanese D (2018) Sensitive detection of *Escherichia coli* O157:H7 in food products by impedimetric immunosensors. Sensors 18:2168. https://doi.org/10.3390/s18072168
24. Hu X, Li Y, Xu Y, Gan Z, Zou X, Shi J, Huang X, Li Z, Li Y (2021) Green one-step synthesis of carbon quantum dots from orange peel for fluorescent detection of *Escherichia coli* in milk. Food Chem 339:127775. https://doi.org/10.1016/j.foodchem.2020.127775
25. Chandra S, Mahto TK, Chowdhuri AR, Das B, Sahu SK (2017) One step synthesis of functionalized carbon dots for the ultrasensitive detection of *Escherichia coli* and iron (III). Sens Actuators B Chem 245:835–844. https://doi.org/10.1016/j.snb.2017.02.017
26. Jiang T, Song Y, Wei T, Li H, Du D, Zhu M-J, Lin Y (2016) Sensitive detection of *Escherichia coli* O157:H7 using Pt–Au bimetal nanoparticles with peroxidase-like amplification. Biosens Bioelectron 77:687–694. https://doi.org/10.1016/j.bios.2015.10.017
27. Idil N, Hedström M, Denizli A, Mattiasson B (2017) Whole cell based microcontact imprinted capacitive biosensor for the detection of *Escherichia coli*. Biosens Bioelectron 87:807–815. https://doi.org/10.1016/j.bios.2016.08.096
28. Zheng L, Cai G, Wang S, Liao M, Li Y, Lin J (2019) A microfluidic colorimetric biosensor for rapid detection of *Escherichia coli* O157:H7 using gold nanoparticle aggregation and smart phone imaging. Biosens Bioelectron 124–125:143–149. https://doi.org/10.1016/j.bios.2018.10.006
29. Sun J, Warden AR, Huang J, Wang W, Ding X (2019) Colorimetric and electrochemical detection of Escherichia coli and antibiotic resistance based on a p-benzoquinone-mediated bioassay. Anal Chem 91:7524–7530. https://doi.org/10.1021/acs.analchem.8b04997
30. Chen S, Chen X, Zhang L, Gao J, Ma Q (2017) Electrochemiluminescence detection of *Escherichia coli* O157:H7 based on a novel polydopamine surface imprinted polymer biosensor. ACS Appl Mater Interfaces 9:5430–5436. https://doi.org/10.1021/acsami.6b12455